Applied Catalysis B: Environmental 288 (2021) 119979

Contents lists available at ScienceDirect

Applied Catalysis B: Environmental

journal homepage: www.elsevier.com/locate/apcatb

In-Sn alloy core-shell nanoparticles: In-doped SnO_x shell enables high stability and activity towards selective formate production from electrochemical reduction of CO_2

Jigang Wang [a,1], Shunlian Ning [a,1], Mi Luo [a,1], Dong Xiang [a], Wei Chen [b], Xiongwu Kang [a,*], Zheng Jiang [c,d,**], Shaowei Chen [e,*]

[a] New Energy Research Institute, School of Environment and Energy South China University of Technology, Higher Education Mega Center, 382 East Waihuan Road, Guangzhou, 510006, China
[b] State Key Laboratory of Electroanalytical Chemistry, Changchun Institute of Applied Chemistry, Chinese Academy of Sciences, Changchun, 130022, China
[c] Shanghai Advanced Research Institute, Chinese Academy of Sciences, Shanghai, 201210, China
[d] China University of Chinese Academy of Sciences, Chinese Academy of Sciences, Beijing, 100049, China
[e] Department of Chemistry and Biochemistry, University of California, Santa Cruz, Santa Cruz, CA, 95064, USA

ARTICLE INFO

Keywords:
Sn-In alloy
Tin oxide
CO_2 reduction
Operando XANES
Operando Raman spectroscopy

ABSTRACT

SnO_2 has been recognized as excellent catalyst towards formate production from electrochemical CO_2 reduction (CO_2R). However, it is a great challenge to prepare SnO_2 that is stable under the working condition of CO_2R and the active center of the SnO_2-based catalyst towards CO_2R has been illusive. In this work, Sn-In alloy nanoparticles display an $InSn_4$ intermetallic core and an amorphous In-doped tin oxide shell and a CO_2-to-formate faradaic efficiency of 94% and a current density of 236 mA cm^{-2} was achieved at −0.98 V. Operando X-ray absorption and Raman spectroscopy reveal that the In-doped tin oxide shell remains stable under CO_2R condition. Density functional theory calculations indicate that the In-doped tin oxide results in the formation of oxygen vacancy, stabilized tin oxide shell and exergonic pathway for CO_2-to-formate, which might account for the high performance of the catalysts towards CO_2R.

1. Introduction

CO_2 can be transformed into valuable chemical feedstocks and dispatchable fuels by electrochemical reduction in a simple device under ambient condition [1–5]. When renewable energy is utilized, electrochemical CO_2 reduction (CO_2R) delegates a unique sustainable technology to achieve economic and green carbon-neutral cycle and mitigate the environmental issues caused by the greenhouse effect. Electrocatalysts play a vital role in the CO_2R process, which can not only reduce the overpotential and energy input, but also manipulate the selectivity towards desired products [6–12]. Of these, formate is an attractive product from CO_2R, because it is a high-energy-density hydrogen carrier for fuel cells and widely used chemical feedstock [13–17]. Indeed, it has been extensively explored to prepared highly active and stable electrocatalysts towards CO_2 to formate [18–23]. For instance, Li et al. prepared 2D bismuth nanosheets and observed a remarkable performance towards the production of formate by CO_2R due to the exposure of abundant active sites [24,25]. Zeng et al. prepared an In_2O_3-reduced graphene oxide (rGO) nanocomposite, which stabilized the intermediate of formate production, leading to apparent improvement of the CO_2R activity and selectivity towards formate, as compared to In_2O_3 alone [26]. In addition, tin oxide has been recognized as a promising electrocatalyst for CO_2 to formate, due to its non-toxicity, low-cost, and high-selectivity in aqueous electrolytes at a moderate overpotential [27–31]. In an early study, Kumar et al. [32]. prepared porous SnO_2 nanowires and observed a high energy conversion efficiency of CO_2 to formate with a steady Faradaic efficiency (FE) of 80% at −0.8 V vs. reversible hydrogen electrode (RHE), which was ascribed to the abundant grain boundaries within the porous nanowires. In another study, Daiyan et al. [33] prepared SnO_2 nanoparticles by a flame

* Corresponding authors.
** Corresponding author at: Shanghai Advanced Research Institute, Chinese Academy of Sciences, Shanghai, 201210, China.
E-mail addresses: esxkang@scut.edu.cn (X. Kang), jiangzheng@sinap.ac.cn (Z. Jiang), shaowei@ucsc.edu.cn (S. Chen).
[1] These authors contributed equally to this work.

https://doi.org/10.1016/j.apcatb.2021.119979
Received 31 October 2020; Received in revised form 16 January 2021; Accepted 4 February 2021
Available online 13 February 2021

spray-pyrolysis technique, which exhibited a CO_2-to-formate FE of 85% and current density of −23.7 mA cm^{-2} at −1.1 V vs. RHE. Notably, oxygen vacancy has been argued to be crucial in activating CO_2 and maintaining the high activity for formate production [34,35].

It should be noted that tin oxide can be readily converted to metallic tin in the process of CO_2R, and the catalytic activity has been argued to arise from the latter rather than the former [34,36–39]. Nevertheless, both experimental [40] and theoretical invenstigations [41] have shown that tin oxide is superior to metallic tin in the electrocatalytic production of formate from CO_2R, while the latter is more favorable for hydrogen evolution. This suggests that to achieve high catalytic activity and selectivity toward formate production by CO_2R, it is imperative to stabilize the structure of tin oxide-based electrocatalysts [42,43].

Herein, we employ a facile, wet-chemical method to prepare tin-indium (Sn-In) alloy nanoparticles with an $InSn_4$ core and an In-doped thin oxide shell. The metallic core ensures high electrical conductivity, while the In-doping enhances the stability of thin oxide under CO_2R condition, thus achieving remarkably improved activity towards formate production. Electrochemically, the Sn-In alloy nanoparticles exhibits an FE > 90% and current density of 236 mA cm^{-2} toward formate production from CO_2R in 1 M KOH at −0.98 V vs. RHE. Operando X-ray absorption near edge structure (XANES) and Raman spectroscopy measurements show that the In-doped tin oxide remains stable under CO_2R condition and facilitates formate production from CO_2R, as compared to pure tin oxide. Consistent results are obtained by theoretical calculations.

2. Experimental

2.1. Materials

Sodium dodecyl sulfate (SDS, 85%), sodium borohydride ($NaBH_4$, 99%) and ethanol (anhydrous) were purchased from Damao. Tin(II) sulfate ($SnSO_4$, 99%), potassium bicarbonate ($KHCO_3$) and indium(III) chloride ($InCl_3$, 99.995%) of analytical grade were purchased from Aladdin. Hydrochloric acid (HCl, 37%) were obtained from Macklin. CO_2 (purity 99.995%), Ar (purity 99.99%), N_2 (purity 99.99%) and H_2 (purity 99.999%) were obtained from Guangzhou Messer Gas (Guangzhou, China). Deionized water (DI) water was obtained from a Barnstead Nanopure water purification system (18.3 MΩ cm). All chemicals were used without further purification.

2.2. Synthesis of Sn-In alloy nanoparticles

Sn-In alloy nanoparticles were prepared in a one-step procedure in an ice bath (ca. −2 °C) under inert atmosphere. First, SDS was dispersed into 20 mL DI water to form a 96 mM solution in a round bottom flask. To prevent the hydrolysis of $SnSO_4$ and $InCl_3$, the pH of the solution was adjusted to ~2.5 by HCl. $SnSO_4$ and $InCl_3$ (at the molar feed ratio of 3:1) were added into the solution above, followed by the addition of 10 mL of 0.45 M $NaBH_4$ through a syringe pump in 25 min. The reaction solution was constantly stirred at 200 rpm for 30 min in the ice bath under inert atmosphere. The resulting solution was centrifuged (TG16-WS) at 8000 rpm, the precipitates were collected and rinsed 3 times with DI water and ethanol, respectively, through the cyclic dispersing and centrifuging process. Finally, the product was desiccated in a vacuum oven (40 °C) for subsequent use. The collected product was denoted as SnIn-3. Samples at other molar feed ratio of Sn:In (1:1, 2:1, 4:1 and 5:1) were prepared in the same manner and denoted as SnIn-x. Monometallic Sn and In nanoparticles were also prepared by following the same procedure by using only $SnSO_4$ or $InCl_3$ precursors.

2.3. Characterization

The size and lattice fringes of the Sn-In alloy nanoparticles were characterized by high-resolution transmission electron microscopy (TEM, JEOL JEM 2100 F). The crystallographic structures of the samples were revealed by X-ray diffraction spectroscopy (XRD, New D8-Advance, BRUKER-AXS) at the scan rate of 5° min^{-1}. The surface elemental compositions and chemical states were examined by X-ray photoelectron spectroscopy (XPS, ThermoFisher Scientific, K-alpha+). The atomic contents of the samples were determined by inductively coupled plasma-atomic emission spectrometric (ICP-AES) measurements. The elemental distribution and line scans for the samples were acquired by energy-dispersive X-ray (EDX) spectroscopy.

2.4. Operando XANES and Raman measurements

X-ray absorption profiles of Sn K-edge and In K-sedge were acquired at the $BL_{14}W_1$ beamline of the Shanghai Synchrotron Radiation Facility (SSRF), China. The storage ring of SSRF was operated at 3.5 GeV with a maximum injection current of 230 mA. Employing a double-crystal monochromator (DCM) equipped with a Si (311) crystal, the hard X-ray was detuned by 30% to remove the harmonic component of the monochrome beam. The Sn-In alloy nanoparticles obtained above were loaded onto a piece of carbon paper, which was employed as the working electrode. A Ag/AgCl electrode with KCl-saturated aqueous electrolyte was employed as reference electrode, while a platinum wire was utilized as a counter electrode. The 0.1 M $KHCO_3$ electrolyte was saturated with CO_2 by bubbling the gas constantly at 30 mL min^{-1} and each potential was held for 1 h during the data acquisition process. The position of the absorption edge (E°) was calibrated by using a Sn foil, and all the XANES data were collected in the fluorescence mode. Each spectrum was measured two times and the positions of E° were almost identical during the multiple scans, ensuring the repeatability of the data. The operando Raman spectra were acquired with a laser excitation at 532 nm (Thermo fisher scientific, DXR2xi).

2.5. Electrochemical measurements

Electrocatalytic performances of these catalysts towards CO_2R were first evaluated in a H-type cell with two compartments separated by a Nafion film by utilizing a three-electrode setup in a 0.1 M $KHCO_3$ electrolyte (CO_2-saturated, pH = 6.8). The Ag/AgCl electrode was employed as the reference electrode and a platinum wire as counter electrode. CO_2 was constantly pumped into the cathode chamber at a rate of 24 mL min^{-1}. The output of the gas flow from the cathode chamber was directed into a gas chromatograph instrument (GC, Huaai 9560) for identification and quantification of the gaseous products, which was purged for 30 min before the start of experiments. A homogeneous catalyst ink was arranged by dispersing 1 mg of carbon supported Sn-In alloy nanoparticles and 10 μL of Nafion solution (5 wt%) into a water-ethanol solution (1:1 in volume) to form a 1 mg/mL solution. The catalyst ink was added dropwise onto a piece of carbon paper (1 × 0.5 cm^2) and the solvent was allowed to evaporate naturally. During the CO_2R experiments, the catholyte was stirred at 500 rpm. Linear sweep voltammetry (LSV) was conducted at a scan rate of 10 mV s^{-1} from −0.3 to −1.4 V vs. RHE. The geometric and specific current density were obtained by normalizing the current to the geometric surface area of the carbon paper and electrochemical surface area (ECSA) of the Sn-In catalysts obtained by double layer capacitance. The liquid products were analyzed by using a Bruker AVANCE III 400 MHz nuclear magnetic resonance (NMR) instrument and phenol was added into the deuterated water solvent as an internal standard.

The Faradaic efficiency of each product from CO_2R was determined by the following equation, $FE = Q_i/Q_t = (N_i \times n \times F)/Q_t$, where Q_t stands for the total charge consumed, Q_i represents the charge reducing a certain product, N_i is the amount of moles of the product (measured by NMR and GC), n is the number of electrons transferred in the elementary reaction (which is 2 for CO, H_2 and HCOOH), and F denotes the Faradaic constant (96,485 C mol^{-1}). The half − cell energy efficiency (EE) for CO_2R to formate was calculated by the following equation: $EE_{half\text{-}cell}$ =

$FE_{formate}$*(1.23-E^0)/(1.23-E), where E^0 = −0.2 V vs. RHE and E is the applied potential.

2.6. Flow cell measurements

The electrochemical performance of the Sn-In alloy catalysts on gas diffusion electrode (GDL, 2 × 1.5 cm^2) was carried out in a custom-designed flow cell reactor. The Sn-In alloy nanoparticles-coated carbon paper with a microporous layer (Sigracet 29 BCE, Fuel Cell Store) was applied as the GDL cathode and a 20 wt% IrO_2/C-loaded carbon paper as the GDL anode. Ag/AgCl in KCl saturated aqueous electrolyte was employed as the reference electrode. The catholyte and anolyte chambers were separated by an anion exchange membrane (SELEMION, 2 × 1.5 cm^2). During the measurements, the flow rate of CO_2 into the cathode GDL was 20 mL min^{-1} and flow rate of the catholyte (1 M $KHCO_3$ or 1 M KOH) were controlled to be 65 rpm via a peristaltic pump (Cole-Parmer).

2.7. Computational studies

Theoretical calculations based on the Pseudopotential Plane-wave (PP-PW) density functional theory (DFT) were carried out via the CASTEP package in Material Studio R17.2. The Perdew-Burke-Ernzerh (PBE) functionals of generalized gradient approximation (GGA) were employed for the electron exchange-correlation. The SnO_2 (110) and In-doped SnO_2 (In-SnO_2) slabs were modeled with a 3 × 2 periodic cell, 4 atomic layers and SnO_2 (110) surface with 2 In atoms substituting Sn atoms on the surface, and the vacuum space on top of the slabs was 20 Å. The energy cut-off, convergence in the energy and forces were set to be 400 eV, 1 × 10^{-5} eV per atom and 0.03 eV $Å^{-1}$, respectively. The self-consistent field tolerance was set to be 1 × 10^{-5} eV, the maximum translation was 0.001 Å and a 3 × 3 × 1 k-point mesh was adopted. In all the metal oxide slabs, the bottom layer of these two models were fixed and the top layers were free to move during the calculation.

The oxygen vacancy formation energy (E_f) can be described as E_f = $E_{(In\text{-}SnO2\text{-}Vo)}$ + $E_{(1/2\ O2)}$ - $E_{(In\text{-}SnO2)}$. The more negative E_f is, the more spontaneous the reaction is, and the more conducive to the formation of oxygen vacancies [44]. The Gibbs free energy (△G) of an elementary reaction is defined as △G = △E + △E_{ZPE} –T△S, where △E is defined by the relationship △E = $E_{ads+surf}$− (E_{ads} + E_{surf}), where $E_{ads+surf}$ represents the total energy of the adsorbate interacting with the substrate slab, E_{ads} is the energy of the gaseous adsorbate, and E_{surf} symbolizes the

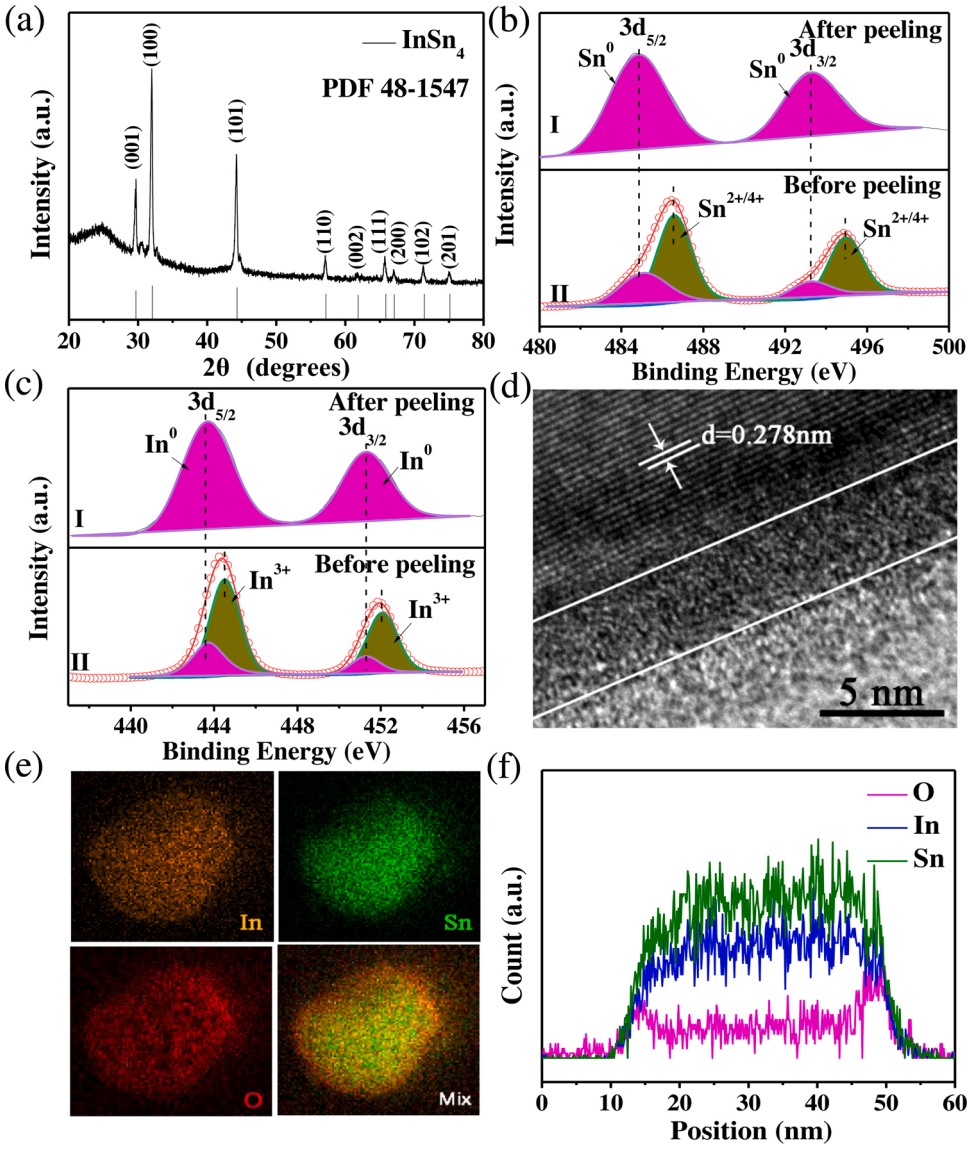

Fig. 1. (a) XRD patterns of SnIn-3 alloy nanoparticles. XPS profiles of the (b) Sn 3d and (c) In 3d electrons of SnIn-3 nanoparticles before and after Ar ion peeling. (d) HRTEM images of SnIn-3 nanoparticles. (e) EDX elemental maps for In, Sn and O, and (f) line scans of SnIn-3 alloy nanoparticles.

energy of the substrate. $\triangle E_{ZPE}$ represents the variance of the zero-point energy from the initial to the final state, and $T\triangle S$ symbolizes the entropy variance of the elementary reaction.

3. Results and discussion

3.1. Characterization of the samples

The Sn-In alloy nanoparticles were prepared by a facile, wet-chemical method, whereby $SnSO_4$ and $InCl_3$ at varied Sn:In molar ratios were reduced by $NaBH_4$, as detailed in the Supporting Information. The crystalline structure of the resulting Sn-In alloy nanoparticles was examined by XRD measurements. From Fig. 1a, SnIn-3 (the sample prepared at the Sn:In molar ratio of 3:1) exhibit a series of well-defined diffraction peaks that are indexed to $InSn_4$ (JCPDS: 48-1547) at 2θ = 29.7° (001), 32.0° (100), 44.3° (101), 57.1° (110), 65.8° (111), 67.0° (200), 71.4° (102), and 75.1° (201). The peak between 20° and 30° is the noise of the instrument. The surface valence states of Sn and In were then examined by XPS. Fig. 1b-c depicts the high-resolution XPS scans of the In 3*d* and Sn 3*d* electrons of the SnIn-3 alloy nanoparticles, respectively. Deconvolution of the Sn 3*d* spectrum (Fig. 1b, bottom curve) yields two doublets at 486.9/495.3 eV and 485.1/493.5 eV, which are ascribed to the $3d_{3/2}/3d_{5/2}$ electrons of $Sn^{2+/4+}$ and Sn°, respectively [35].

Similarly, the In 3*d* spectra (Fig. 1c, bottom curve) also entailed two doublets at 444.2/451.7 eV and 443.4/450.9 eV, which are ascribed to the $3d_{3/2}/3d_{5/2}$ electrons of In^{3+} and In°, respectively [45]. Interestingly, when the surface layer of the SnIn-3 alloy nanoparticles was removed by Ar ion beams, only metallic Sn and In can be seen (top curves of Fig. 1b and c, and Fig. S1), suggesting that the SnIn-3 nanoparticles consist of a metallic $InSn_4$ core and a mixed In-Sn oxide shell.

Note that the overall atomic ratio of Sn to In in SnIn-3 was calculated to be 2.81 by ICP-AES measurements, somewhat higher than that (2.38) estimated by XPS measurements (Table S1), suggesting that the surface of the SnIn-3 alloy nanoparticles was dominated by tin oxide with about 29.6% In dopants. The morphology of the SnIn-3 alloy nanoparticles was then characterized by TEM measurements. From Fig. S2, one can see that the nanoparticles display a spherical shape, with an average particle diameter of ca. 37 nm. From the electron diffraction pattern (Fig. S2 inset), crystal phase (100), (110) and (201) were clearly observed, which matched with the $InSn_4$ alloy structure from the XRD measurement. HRTEM images (Fig. 1d) show that the nanoparticles exhibit well-defined lattice fringe of 0.278 nm, which is in line with the (100) facets of $InSn_4$, and an amorphous oxide layer of approximately 3 nm. Fig. 1e-f display the elemental maps and line scans of In, Sn and O based on EDX, where the O species are enriched on the surface, while Sn and In are distributed rather evenly throughout the entire particle, further confirming the formation of a core-shell structure of the SnIn-3 alloy

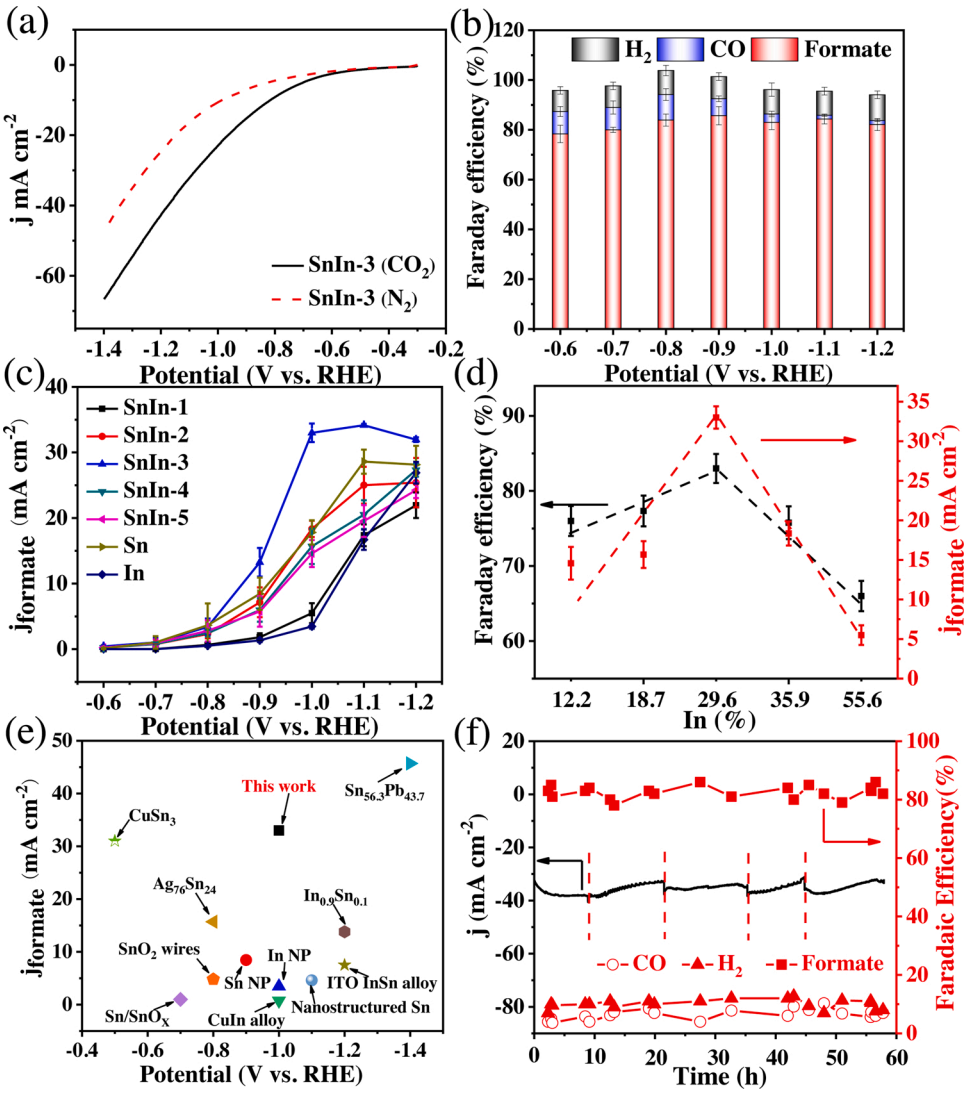

Fig. 2. (a) LSV curves of SnIn-3 in N_2- (red dashed line) and CO_2- (black solid line) saturated 0.1 M $KHCO_3$ at the scan rate of 10 mV s^{-1}. (b) FE of formate, CO and H_2 on SnIn-3. (c) Partial current densities of formate on Sn-In, Sn and In nanoparticles. (d) Variation of FE and $j_{formate}$ with the indium content on the surface of Sn-In alloy nanoparticles at −1.0 V vs. RHE. (e) Current density of CO_2 to formate of the catalysts reported in the literature. (f) Stability test of SnIn-3 at −1.0 V for 58 h. The dotted lines refer to the replacement of fresh electrolyte.

nanoparticles, as suggested above in XPS and TEM measurements.

3.2. Electrocatalytic performance for CO_2R

The electrocatalytic activity of the SnIn-3 alloy nanoparticles towards CO_2R was first examined in a H-type cell employing a typical three-electrode setup. As shown in Fig. 2a, the current density of SnIn-3 acquired by LSV is significantly higher than that when the electrolyte solution was N_2-purged, indicative of apparent CO_2R activity. Remarkably, formate is the dominant product of CO_2R, with an FE of over 80% in a potential range from −0.6 to −1.2 V vs. RHE, which reaches a maximum of 86% at −0.9 V vs. RHE, whereas CO and H_2 account for only a small fraction of the final products (Fig. 2b).

For comparison, Sn-In alloy nanoparticles were also prepared in the same manner at other Sn:In feed ratios (i.e., 1:1, 2:1, 4:1 and 5:1), which were denoted as SnIn-1, SnIn-2, SnIn-4 and SnIn-5, respectively, along with monometallic Sn and In nanoparticles (details in the Supporting Information). In comparison to SnIn-3, SnIn-1 and SnIn-2 exhibit well-defined XRD patterns of indium at $2\theta = 32.9^\circ$ (101), 36.3° (002), and 39.1° (110), due to the increasing In content in the alloy nanoparticles (Fig. S3). In fact, SnIn-1 is dominated with metallic In, and only very weak peaks of $InSn_4$ was observed. For SnIn-4 and SnIn-5, the increasing Sn component led to enhanced diffraction peaks at $2\theta = 30.6^\circ$ (200), 43.8° (220), 44.9° (211), 55.3° (301), 62.5° (112) and 64.5° (321), due to metallic Sn, in addition to those from $InSn_4$, which is in line with the phase diagram of the bulk Sn-In [46].

The CO_2R performance of these Sn-In alloy nanoparticles was then evaluated and compared (Fig. S4). For SnIn-1 sample (Fig. S4b), current density for CO_2R emerges at potential of −0.8 V and FE for formate production reaches maximum of 74% at −1.1 V, with minute quantities of CO in a broad potential range. Since SnIn-1 consisted mainly of metallic In, the electrochemical performance was indeed similar to that by In (Fig. S4a). Notably, SnIn-3 was the best among these samples within the context of FE and current density, and the Sn-In alloy nanoparticles all outperformed Sn alone (Fig. S4−5).

The partial current density of formate ($j_{formate}$) on the various nanoparticle catalysts was then quantified and shown in Fig. 2c, which can be seen to increase markedly with increasingly negative potential, but decreases somewhat at potentials beyond −1.1 V, which was likely limited by CO_2 diffusion [35]. Clearly, SnIn-3 alloy nanoparticles display the highest partial current density among the series of samples, which reaches a maximum of 34.15 mA cm^{-2} at −1.1 V, about 1.8 times that of Sn (17.8 mA cm^{-2}) and 9.5 times that of In (3.4 mA cm^{-2}). Interestingly, the CO_2-to-formate FE and current density on the Sn-In alloy nanoparticles display a volcano-shaped dependence on the surface content of indium (Table S1), with SnIn-3 (29.6%) as the optimal catalyst within the current experimental context (Fig. 2d). It is anticipated and demonstrated by DFT calculation that the oxygen vacancies created by In-doping in SnO_2 and In-site in In-doped SnO_2 are responsible for the high performance of CO_2R in SnIn-3. However, Sn-In alloys with any other Sn-In feed ratios exhibit pure In or Sn, which could result in pure SnO_2 or In_2O_3 and has been demonstrated less stable and active than In-doped SnO_2. It can be envisioned that the low In-doping level may result in low concentration of oxygen vacancy and In sites in SnO_2 and thus low CO_2R activity. On other hand, if the In-doping level is high, then the Sn-In alloys surface might be mainly consisted of In_2O_3, which also disfavor CO_2R. Thus, the catalytic performance of Sn-In alloy towards CO_2R is maximized at a certain ratio. Compared to relevant catalysts reported in the literature, SnIn-3 nanoparticles outperform a large number of literature catalysts, exhibiting a high $j_{formate}$ for CO_2R to formate (Fig. 2e).

The specific activity of the catalysts was also evaluated by normalizing the current density to ECSA, which was determined by double layer capacitance (C_{dl}, Fig. S6 and Table S2). The trend of the specific activity is in line with that of the geometric current density (Fig. S7a). SnIn-3 still exhibits the largest specific current dnesity for formate productoin. The cathodic EE of the formate formation on SnIn-3 alloy catalyst was then calculated and compared to relevant catalysts reported in the literature (Fig. S7b). Clearly, SnIn-3 nanoparticles outperform a large number of literature catalysts, exhibiting a high EE (61.2%) for CO_2R to formate. In comparison to leading results in the literature, the SnIn-3 catalyst is one of the best electrocatalysts for CO_2-to-formate in terms of activity and selectivity of formate production, as illustrated in Table S4.

The electron-transfer kinetics for CO_2R was then assessed by the Tafel plot of the formate partial currents [47,48]. In Fig. S7c and Table S2, the Tafel slope for SnIn-3 is estimated to be 175 mV dec^{-1}, the lowest among the series of samples, in comparison to 213 mV dec^{-1} for SnIn-1, 205 mV dec^{-1} for SnIn-2, 214 mV dec^{-1} for SnIn-4, 230 mV dec^{-1} for SnIn-5, 220 mV dec^{-1} for Sn, and 217 mV dec^{-1} for In. This suggests that SnIn-3 displays the fastest reaction kinetics [49] and the rate determining step (RDS) is the process of the first electron-transfer to the adsorbed CO_2. Furthermore, the smaller interfacial charge transfer resistance (R_{ct}) measured by the electrochemical impedance spectra (EIS, Fig. S8) indicate the lowest interfacial charge-transfer resistance on SnIn-3 catalysts and thus the highest catalytic activity towards CO_2R. As the adsorption of OH^- can be considered as a surrogate for $CO_2^{\bullet-}$ [34,36,50,51], one can see that SnIn-3 displays more negative potential for OH^- adsorption than Sn and In (Fig. S7d), indicating a stronger binding of $CO_2^{\bullet-}$ ions on SnIn-3, indicating that SnIn-3 is more conducive to stabilizing CO_2^{*-} intermediate, thus benefiting the overall CO_2 reduction, consistent with the superior CO_2R activity on the SnIn-3 alloy nanoparticles. In addition, the current density on SnIn-3 remains virtually invariant at −1.0 V for 58 h in 0.1 M $KHCO_3$ electrolyte (Fig. 2f), indicating excellent activity and stability of SnIn-3 towards formate production by CO_2R.

3.3. Impact of the In-doping on the catalyst

As mentioned earlier, the Sn-In alloy nanoparticles are composed of an $InSn_4$ metallic core encapsulated with an In-doped tin oxide shell. It has been reported that tin oxides could be reduced to metallic tin under CO_2R condition [34,36–38]. Thus, one may ask if the In-doped tin oxide shell on $InSn_4$ survives during CO_2R and what the actual active sites are for the Sn-In alloy nanoparticles. Therefore, the valence states and local structure of the Sn-In alloy nanoparticles were then examined by using operando XANES measurements (Fig. S9a), where the cathode was biased at several selected potentials from the open circuit potential (OCP) down to −1.2 V. Each potential was kept for more than 20 min before XANES measurements to ensure that the catalyst reached the steady state. From the Sn K-edge XANES profile in Fig. 3a, one can see that the SnIn-3 nanoparticles (at OCP) exhibited a white line energy of 29214.2 eV, lower than that (29215.7 eV) of SnO_2, but higher than that (29211.2 eV) of Sn foil, suggesting that the valence state of Sn in SnIn-3 is in the intermediate between 0 and +4. Consistent results can be obtained from the white line intensity, which also varied in the order of Sn foil < SnIn-3 (OCP) < SnO_2. Intriguingly, the XANES profiles and hence the Sn oxidation state in SnIn-3 remains practically unchanged with the cathode potential varied from OCP to −1.2 V for 1 h, indicating extraordinary stability of the catalyst. Very similar behaviors were observed with the In K-edge XANES profiles (Fig. 3b). These results suggest high structural stability of the In-doped tin oxide shell during CO_2R, which most likely acted as the actual active centers.

This is further confirmed in operando Raman spectroscopy measurements (Fig. 3c and d, Fig. S9b and c). From Fig. 3c and d, one can see that in both SnIn-3 and Sn nanoparticles, the Sn-O vibrational bands appeared at 113 (B_{1g}) and 206 cm^{-1} (A_{1g}) [52]. Since the vibrational wavenumbers of In-O and Sn-O bond are close to each other and In only accounts for a low concentration in the sample, the In-O bonds are undistinguished from Sn-O. Remarkably, one can see that for the SnIn-3 alloy nanoparticles, the Sn-O/In-O bands remained unchanged even after CO_2R operation at −0.6 V for 1 h, and became only slightly

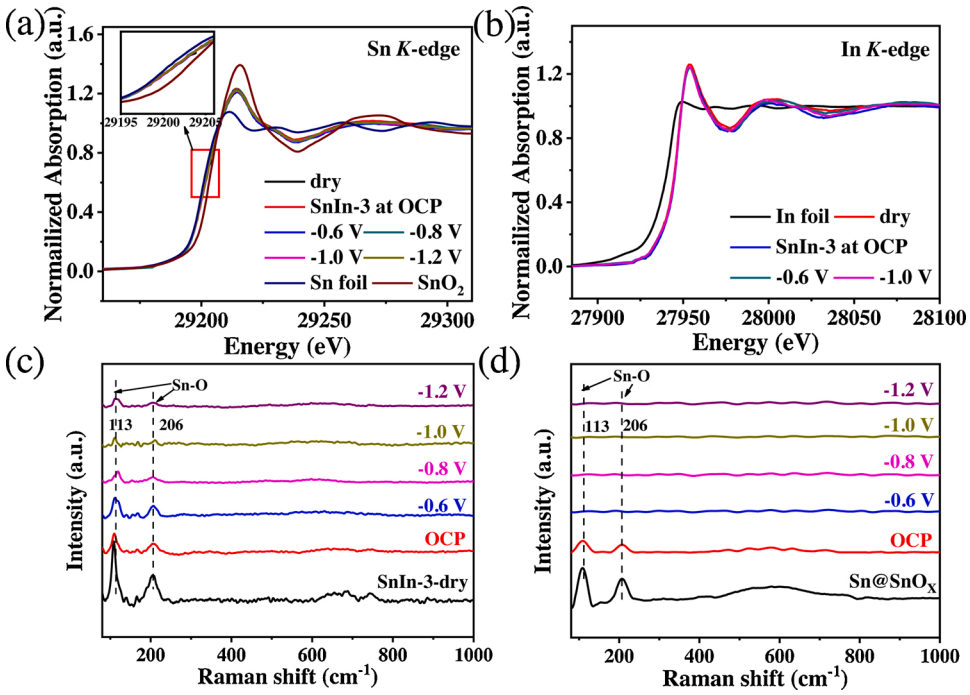

Fig. 3. Operando XANES profiles of (a) Sn and (b) In K-edge of SnIn-3 alloy nanoparticles at different potentials. The inset to panel (a) is the zoom in of the pre-edge spectra of Sn K-edge. Operando Raman spectra of (c) SnIn-3 alloy nano-particles and (d) Sn@SnO_X nanoparticles at different potentials under CO_2R.

attenuated at more negative potentials of −0.8, −1.0 and −1.2 V, again, indicating its extraordinary stability under CO_2R condition [53]. By contrast, the Sn-O vibrational bands from the oxide shell of mono-metallic Sn nanoparticles disappeared very quickly, due to facile reduction of tin oxide to metallic Sn under CO_2R potentials. Temperature-programmed reduction by hydrogen experiments (Fig. S10) indicate that, among three samples, In-doping can stabilize surface oxygen species and improve the stability of the oxide against the hydrogen reduction, further corroborating the results from operando Raman and XANES. Taken together, results from the operando XANES and Raman measurements suggest that the SnIn-3 alloy nanoparticles exhibited a robust tin oxide shell, which most likely served as the actual active component for CO_2R to formate.

The CO_2R performance of the SnIn-3 nanoparticles was also tested in

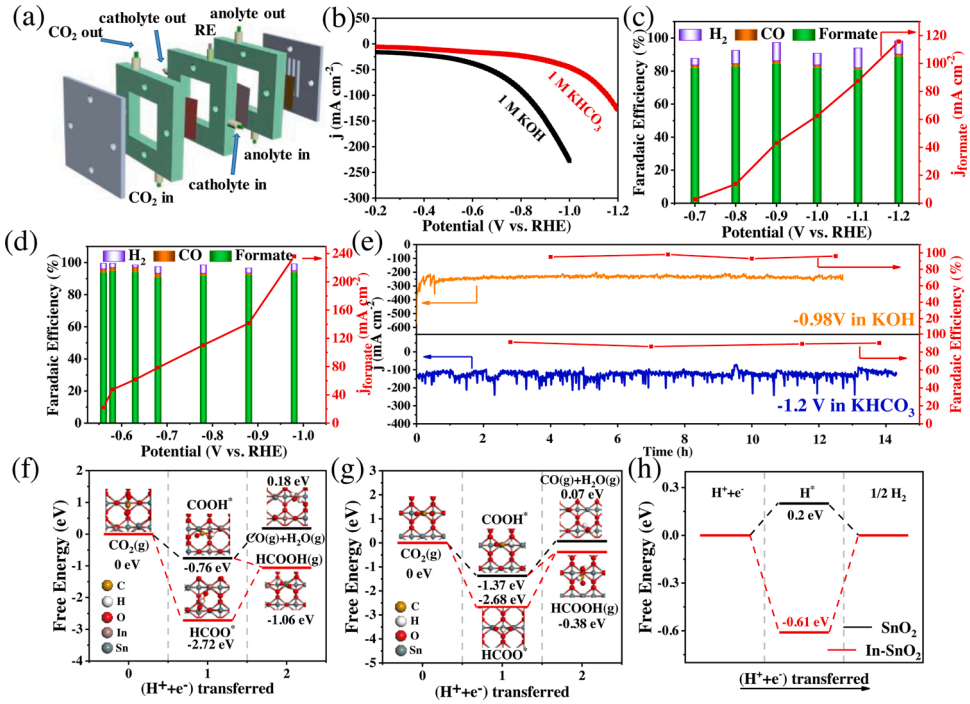

Fig. 4. (a) Schematic illustration and (b) polarization curves of SnIn-3 alloy nanoparticles in 1 M $KHCO_3$ and 1 M KOH. FE and partial current density of CO_2R on SnIn-3 in.(c) 1 M $KHCO_3$ and (d) 1 M KOH solution. (e) Long-term i-t profiles in 1 M $KHCO_3$ and KOH electrolyte. Gibbs free energy diagrams of CO_2 to formate (red) and CO (gray) pathways on (f) In-SnO_2 and (g) pure SnO_2. (h) Free energy diagram of HER on SnO_2 and In-doped SnO_2.

a flow cell reactor (Fig. 4a and b), where a $j_{formate}$ of 116 mA cm^{-2} and an FE of 89% were otained for formate production at −1.2 V (Fig. 4c). Notably, the CO_2R activity of the Sn-In alloy nanoparticles in alkaline electrolyte (1 M KOH) is higher than in neutral electrolyte (1 M $KHCO_3$) since hydroxide ions can suppress the competing HER and lower the CO_2 activation energy barrier [25]. For instance, the onset potential of CO_2R decreases from −0.7 V in 1 M $KHCO_3$ to −0.4 V in 1 M KOH (Fig. 4b), and the $j_{formate}$ and FE of formate increased to 236 mA cm^{-2} and 94% at −0.98 V in the latter (Fig. 4d) (yet for practical applications, $KHCO_3$ is preferred in that it is less corrosive). The SnIn-3 nanoparticle catalysts also exhibited excellent stability at high current density. For instance, the current density remained unchanged at 251 mA cm^{-2} at −0.98 V in 1 M KOH for 12 h, and at 130 mA cm^{-2} at −1.2 V in 1 M $KHCO_3$ for 14 h (Fig. 4e).

3.4. DFT theoretical calculation

DFT calculations were then performed to reveal the root cause of the enhanced activity of the target catalyst. Both pristine SnO_2 (110) and In-doped SnO_2 (110) were utilized to model the surfaces of pure Sn and SnIn-3 alloy nanoparticles (Fig. S11), respectively. One can see that that In doping in SnO_2 results in the formation of oxygen vacancy, which has been known to be beneficial to formate production from CO_2R [30,54]. Indeed, from Fig. S10 and Table S3, one can see that the formation energy of oxygen vacancy on In-SnO_2 (−1.90 to −2.08 eV) is reduced compared to that of pristine SnO_2 (−2.23 eV).

To unravel the energetics and reaction pathways of CO_2R for CO and formate production (Fig. S12 and S13), the free energy diagrams on In-SnO_2 and SnO_2 are constructed and presented in Fig. 4f and g [55,56]. Both COOH* and HCOO* are important intermediates for formate production, and the formation of formate through COOH* intermediate is a spontaneous, exothermic process on In-SnO_2[57,58], whereas an energy barrier of 0.99 eV is found on SnO_2. In the other pathway, the energy barrier from HCOO* to HCOOH is much lower on In-SnO_2 (1.66 eV) than that on SnO_2 (2.30 eV), indicating that formate is favored on In-SnO_2 in both pathways. DFT calculations also indicate that hydrogen adsorption on In-SnO_2 (−0.61 eV) is markedly stronger than that on SnO_2 (0.2 eV), which not only suppresses the HER process, but also provide abundant adsorbed hydrogen for formate production (Fig. 4h).

4. Conclusion

In summary, Sn-In alloy nanoparticles (dia. 37 nm) were prepared via a facile, wet-chemical method, and microscopic and spectroscopic characterizations suggested the formation of an $InSn_4$ alloy core encapsulated with an In-doped tin oxide shell. The sample (SnIn-3) prepared at the Sn:In feed ratio of 3:1 exhibited the best CO_2R performance in the selective production of formate, among the series of samples. Specifically, the SnIn-3 alloy nanoparticles exhibited a high FE in a potential window from −0.6 to −1.2 V and a current density of 34.15 mA cm^{-2} for formate production at −1.1 V. By employing GDL in a flow cell and 1 M KOH electrolyte, a current density of 251 mA cm^{-2} and an FE of 94% were obtained for formate production at −0.98 V. Operando XANES and Raman measurements indicate that the In-doped tin oxide shell remained structurally intact during CO_2R and most likely served as the active component for CO_2R to formate. DFT calculations indeed confirmed that In-doping results in the formation of oxygen vacancy, which was conducive to stabilize the rest of the oxygen components in tin oxide and promote the formate production due to the optimized energetics of the important reaction intermediates, as compared to pristine tin oxide. Results from the present study highlight the significance of structural engineering in the manipulation and optimization of tin-based electrocatalysts towards the selective production of formate from CO_2R. Such fundamental insights may be exploited for advacing the low-cost, high-performance metal oxide-based catalysts for electrochemical energy conversion.

CRediT authorship contribution statement

Jigang Wang: Investigation, Formal analysis, Writing - original draft. **Shunlian Ning:** DFT calculations. **Mi Luo:** Operando XANES measurements, Formal analysis. **Dong Xiang:** Operando XANES measurements. **Wei Chen:** Investigation, Funding acquisition. **Xiongwu Kang:** Supervision, Conceptualization, Data curation, Writing - review & editing, Funding acquisition. **Zheng Jiang:** Operando XANES measurements, Data curation. **Shaowei Chen:** Supervision, Data curation, Writing - review & editing.

Declaration of Competing Interest

The authors report no declarations of interest.

Acknowledgements

This work was supported by the National Natural Science Foundation of China (No. U2032151 and 21773224), National Key R&D Program of China (No. 2018YFB1502600) and the Fundamental Research Funds for Central Universities (SCUT Grant No. 2019ZD22).

Appendix A. Supplementary data

Supplementary data associated with this article can be found, in the online version, at https://doi.org/10.1016/j.apcatb.2021.119979.

References

[1] A.M. Appel, J.E. Bercaw, A.B. Bocarsly, H. Dobbek, D.L. DuBois, M. Dupuis, J. G. Ferry, E. Fujita, R. Hille, P.J.A. Kenis, C.A. Kerfeld, R.H. Morris, C.H.F. Peden, A. R. Portis, S.W. Ragsdale, T.B. Rauchfuss, J.N.H. Reek, L.C. Seefeldt, R.K. Thauer, G. L. Waldrop, Frontiers, opportunities, and challenges in biochemical and chemical catalysis of CO_2 fixation, Chem. Rev. 113 (2013) 6621–6658.
[2] S. Verma, B. Kim, H.-R.M. Jhong, S. Ma, P.J.A. Kenis, A gross-margin model for defining technoeconomic benchmarks in the electroreduction of CO_2, ChemSusChem 9 (2016) 1972–1979.
[3] S. Chu, Y. Cui, N. Liu, The path towards sustainable energy, Nat. Mater. 16 (2016) 16.
[4] S.-G. Han, D.-D. Ma, S.-H. Zhou, K. Zhang, W.-B. Wei, Y. Du, X.-T. Wu, Q. Xu, R. Zou, Q.-L. Zhu, Fluorine-tuned single-atom catalysts with dense surface Ni-N4 sites on ultrathin carbon nanosheets for efficient CO_2 electroreduction, Appl. Catal. B 283 (2021), 119591.
[5] X. Zhang, Z. Chen, M. Jiao, X. Ma, K. Mou, F. Cheng, Z. Wang, X. Zhang, L. Liu, Defects and conductive nitrogen-carbon framework regulated ZnInOx nanosheets for boosting CO_2 electrocatalytic reduction, Appl. Catal. B 279 (2020), 119383.
[6] M.B. Ross, P. De Luna, Y. Li, C.-T. Dinh, D. Kim, P. Yang, E.H. Sargent, Designing materials for electrochemical carbon dioxide recycling, Nat. Catal. 2 (2019) 648–658.
[7] S. Shen, C. Han, B. Wang, Y. Du, Y. Wang, Dual active sites-dependent syngas proportions from aqueous CO_2 electroreduction, Appl. Catal. B 279 (2020), 119380.
[8] M.T. Tang, H. Peng, P.S. Lamoureux, M. Bajdich, F. Abild-Pedersen, From electricity to fuels: descriptors for C1 selectivity in electrochemical CO_2 reduction, Appl. Catal. B 279 (2020), 119384.
[9] Z. Chen, M.-R. Gao, N. Duan, J. Zhang, Y.-Q. Zhang, T. Fan, J. Zhang, Y. Dong, J. Li, Q. Liu, X. Yi, J.-L. Luo, Tuning adsorption strength of CO_2 and its intermediates on tin oxide-based electrocatalyst for efficient CO_2 reduction towards carbonaceous products, Appl. Catal. B 277 (2020), 119252.
[10] Z. Chen, T. Wang, B. Liu, D. Cheng, C. Hu, G. Zhang, W. Zhu, H. Wang, Z.-J. Zhao, J. Gong, Grain-boundary-Rich copper for efficient solar-driven electrochemical CO_2 reduction to ethylene and ethanol, J. Am. Chem. Soc. 142 (2020) 6878–6883.
[11] W.J. Dong, C.J. Yoo, J.-L. Lee, Monolithic nanoporous in–Sn alloy for electrochemical reduction of carbon dioxide, ACS Appl. Mater. Interfaces 9 (2017) 43575–43582.
[12] S. Kim, W.J. Dong, S. Gim, W. Sohn, J.Y. Park, C.J. Yoo, H.W. Jang, J.-L. Lee, Shape-controlled bismuth nanoflakes as highly selective catalysts for electrochemical carbon dioxide reduction to formate, Nano Energy 39 (2017) 44–52.
[13] X. Lu, D.Y.C. Leung, H. Wang, M.K.H. Leung, J. Xuan, Electrochemical reduction of Carbon Dioxide to formic acid, ChemElectroChem 1 (2014) 836–849.
[14] X. Yu, P.G. Pickup, Recent advances in direct formic acid fuel cells (DFAFC), J. Power Sources 182 (2008) 124–132.
[15] A.S. Agarwal, Y. Zhai, D. Hill, N. Sridhar, The electrochemical reduction of carbon dioxide to formate/formic acid: engineering and economic feasibility, Chemsuschem 4 (2011) 1705.

[16] B. Wei, Y. Xiong, Z. Zhang, J. Hao, L. Li, W. Shi, Efficient electrocatalytic reduction of CO_2 to HCOOH by bimetallic In-Cu nanoparticles with controlled growth facet, Appl. Catal. B 283 (2021), 119646.

[17] C.J. Yoo, W.J. Dong, J.Y. Park, J.W. Lim, S. Kim, K.S. Choi, F.O. Odongo Ngome, S.-Y. Choi, J.-L. Lee, Compositional and geometrical effects of bimetallic Cu–Sn catalysts on selective electrochemical CO_2 reduction to CO, Acs Appl. Energy Mater. 3 (2020) 4466–4473.

[18] J.-H. Guo, W.-Y. Sun, Integrating nickel-nitrogen doped carbon catalyzed CO_2 electroreduction with chlor-alkali process for CO, Cl_2 and $KHCO_3$ production with enhanced techno-economics, Appl. Catal. B 275 (2020), 119154.

[19] F. Li, G.H. Gu, C. Choi, P. Kolla, S. Hong, T.-S. Wu, Y.-L. Soo, J. Masa, S. Mukerjee, Y. Jung, J. Qiu, Z. Sun, Highly stable two-dimensional bismuth metal-organic frameworks for efficient electrochemical reduction of CO_2, Appl. Catal. B 277 (2020), 119241.

[20] M. Fan, S. Prabhudev, S. Garbarino, J. Qiao, G.A. Botton, D.A. Harrington, A. C. Tavares, D. Guay, Uncovering the nature of electroactive sites in nano architectured dendritic Bi for highly efficient CO_2 electroreduction to formate, Appl. Catal. B 274 (2020), 119031.

[21] C. Hu, L. Li, W. Deng, G. Zhang, W. Zhu, X. Yuan, L. Zhang, Z.-J. Zhao, J. Gong, Selective electroreduction of Carbon Dioxide over SnO_2-Nanodot catalysts, ChemSusChem (2020) n/a.

[22] W. Zhu, L. Zhang, S. Liu, A. Li, X. Yuan, C. Hu, G. Zhang, W. Deng, K. Zang, J. Luo, Y. Zhu, M. Gu, Z.-J. Zhao, J. Gong, Enhanced CO_2 electroreduction on neighboring Zn/Co monomers by electronic effect, Angew. Chem.-Int. Edit. 59 (2020) 12664–12668.

[23] J.W. Lim, W.J. Dong, J.Y. Park, D.M. Hong, J.-L. Lee, Spontaneously formed CuSx catalysts for selective and stable electrochemical reduction of industrial CO_2 gas to formate, ACS Appl. Mater. Interfaces 12 (2020) 22891–22900.

[24] H. Yang, N. Han, J. Deng, J. Wu, Y. Wang, Y. Hu, P. Ding, Y. Li, Y. Li, J. Lu, Selective CO_2 reduction on 2D mesoporous Bi nanosheets, Adv. Energy Mater. 8 (2018), 1801536.

[25] Q. Gong, P. Ding, M. Xu, X. Zhu, M. Wang, J. Deng, Q. Ma, N. Han, Y. Zhu, J. Lu, Z. Feng, Y. Li, W. Zhou, Y. Li, Structural defects on converted bismuth oxide nanotubes enable highly active electrocatalysis of carbon dioxide reduction, Nat. Commun. 10 (2019) 2807.

[26] Z. Zhang, F. Ahmad, W. Zhao, W. Yan, W. Zhang, H. Huang, C. Ma, J. Zeng, Enhanced electrocatalytic reduction of CO_2 via chemical coupling between indium oxide and reduced graphene oxide, Nano Lett. 19 (2019) 4029–4034.

[27] K. Wang, D. Liu, P. Deng, L. Liu, S. Lu, Z. Sun, Y. Ma, Y. Wang, M. Li, B.Y. Xia, C. Xiao, S. Ding, Band alignment in Zn_2SnO_4/SnO_2 heterostructure enabling efficient CO_2 electrochemical reduction, Nano Energy 64 (2019), 103954.

[28] F. Li, L. Chen, G.P. Knowles, D.R. MacFarlane, J. Zhang, Hierarchical mesoporous SnO_2 nanosheets on carbon cloth: a robust and flexible electrocatalyst for CO_2 reduction with high efficiency and selectivity, Angew. Chem.-Int. Edit. 56 (2017) 505–509.

[29] H. Li, N. Xiao, Y. Wang, C. Liu, S. Zhang, H. Zhang, J. Bai, J. Xiao, C. Li, Z. Guo, S. Zhao, J. Qiu, Promoting the electroreduction of CO_2 with oxygen vacancies on a plasma-activated SnOx/carbon foam monolithic electrode, J. Mater. Chem. A 8 (2020) 1779–1786.

[30] F. Wei, T. Wang, X. Jiang, Y. Ai, A. Cui, J. Cui, J. Fu, J. Cheng, L. Lei, Y. Hou, S. Liu, Controllably engineering mesoporous surface and dimensionality of SnO_2 toward high-performance CO_2 electroreduction, Adv. Funct. Mater. (2020), 2002092 n/a.

[31] G. Liu, Z. Li, J. Shi, K. Sun, Y. Ji, Z. Wang, Y. Qiu, Y. Liu, Z. Wang, P. Hu, Black reduced porous SnO_2 nanosheets for CO_2 electroreduction with high formate selectivity and low overpotential, Appl. Catal. B 260 (2020), 118134.

[32] B. Kumar, V. Atla, J.P. Brian, S. Kumari, T.Q. Nguyen, M. Sunkara, J.M. Spurgeon, Reduced SnO_2 porous nanowires with a high density of grain boundaries as catalysts for efficient electrochemical CO_2-into-HCOOH conversion, Angew. Chem.-Int. Edit. 56 (2017) 3645–3649.

[33] R. Daiyan, E.C. Lovell, N.M. Bedford, W.H. Saputera, K.-H. Wu, S. Lim, J. Horlyck, Y.H. Ng, X. Lu, R. Amal, Modulating activity through defect engineering of tin oxides for electrochemical CO_2 reduction, Adv. Sci. 6 (2019), 1900678.

[34] S. Zhang, P. Kang, T.J. Meyer, Nanostructured tin catalysts for selective electrochemical reduction of Carbon Dioxide to formate, J. Am. Chem. Soc. 136 (2014) 1734–1737.

[35] W. Luc, C. Collins, S. Wang, H. Xin, K. He, Y. Kang, F. Jiao, Ag-Sn bimetallic catalyst with a core-shell structure for CO_2 reduction, J. Am. Chem. Soc. 139 (2017) 1885–1893.

[36] D.H. Won, C.H. Choi, J. Chung, M.W. Chung, E.-H. Kim, S.I. Woo, Rational design of a hierarchical tin dendrite electrode for efficient electrochemical reduction of CO_2, ChemSusChem 8 (2015) 3092–3098.

[37] J. Wu, F.G. Risalvato, S. Ma, X.-D. Zhou, Electrochemical reduction of carbon dioxide III. The role of oxide layer thickness on the performance of Sn electrode in a full electrochemical cell, J. Mater. Chem. A 2 (2014) 1647–1651.

[38] Y. Zhang, L. Chen, F. Li, C.D. Easton, J. Li, A.M. Bond, J. Zhang, Direct detection of Electron transfer reactions underpinning the tin-catalyzed electrochemical reduction of CO_2 using fourier-transformed ac voltammetry, ACS Catal. 7 (2017) 4846–4853.

[39] C. Zhao, J. Wang, J.B. Goodenough, Comparison of electrocatalytic reduction of CO_2 to HCOOH with different tin oxides on carbon nanotubes, Electrochem. commun. 65 (2016) 9–13.

[40] Y. Chen, M.W. Kanan, Tin oxide dependence of the CO_2 reduction efficiency on tin electrodes and enhanced activity for Tin/Tin oxide thin-film catalysts, J. Am. Chem. Soc. 134 (2012) 1986–1989.

[41] J. Li, J. Jiao, H. Zhang, P. Zhu, H. Ma, C. Chen, H. Xiao, Q. Lu, Two-dimensional SnO_2 nanosheets for efficient carbon dioxide electroreduction to formate, ACS Sustain. Chem. Eng. 8 (2020) 4975–4982.

[42] G. Wen, B. Ren, M.G. Park, J. Yang, H. Dou, Z. Zhang, Y.-P. Deng, Z. Bai, L. Yang, J. Gostick, G.A. Botton, Y. Hu, Z. Chen, Ternary Sn-Ti-O electrocatalyst boosts the stability and energy efficiency of CO2 reduction, Angew. Chemie Int. Ed. 59 (2020) 12860–12867.

[43] A. Vasileff, C. Xu, Y. Jiao, Y. Zheng, S.-Z. Qiao, Surface and interface engineering in copper-based bimetallic materials for selective CO_2 electroreduction, Chem 4 (2018) 1809–1831.

[44] H. Shiiba, N. Zettsu, M. Nakayama, S. Oishi, K. Teshima, Defect Formation Energy in Spinel $LiNi_{0.5}Mn_{1.5}O_4$-δ Using Ab Initio DFT Calculations, J. Phys. Chem. C 119 (2015) 9117–9124.

[45] Y. Wang, J. Zhao, Y. Li, C. Wang, Selective photocatalytic CO_2 reduction to CH_4 over Pt/In_2O_3: significant role of hydrogen adatom, Appl. Catal. B 226 (2018) 544–553.

[46] C.E.T. White, Phase Diagrams of Indium Alloys and Their Engineering Applications, ASM International, Indium Corporation of America, 1992.

[47] X. Cui, Z. Pan, L. Zhang, H. Peng, G. Zheng, Selective etching of nitrogen-doped carbon by steam for enhanced electrochemical CO_2 reduction, Adv. Energy Mater. 7 (2017), 1701456.

[48] A. Zhang, R. He, H. Li, Y. Chen, T. Kong, K. Li, H. Ju, J. Zhu, W. Zhu, J. Zeng, Nickel doping in atomically thin tin disulfide nanosheets enables highly efficient CO_2 reduction, Angew. Chem.-Int. Edit. 57 (2018) 10954–10958.

[49] S. Gao, Y. Lin, X. Jiao, Y. Sun, Q. Luo, W. Zhang, D. Li, J. Yang, Y. Xie, Partially oxidized atomic cobalt layers for carbon dioxide electroreduction to liquid fuel, Nature 529 (2016) 68.

[50] A. Salehi-Khojin, H.-R.M. Jhong, B.A. Rosen, W. Zhu, S. Ma, P.J.A. Kenis, R. I. Masel, Nanoparticle silver catalysts that show enhanced activity for carbon dioxide electrolysis, J. Phys. Chem. C 117 (2013) 1627–1632.

[51] F. Lei, W. Liu, Y. Sun, J. Xu, K. Liu, L. Liang, T. Yao, B. Pan, S. Wei, Y. Xie, Metallic tin quantum sheets confined in graphene toward high-efficiency carbon dioxide electroreduction, Nat. Commun. 7 (2016) 12697.

[52] C. Li, M. Zheng, X. Wang, L. Yao, L. Ma, W. Shen, Fabrication and ultraviolet photoresponse characteristics of ordered SnOx($x \approx 0.87, 1.45, 2$) nanopore films, Nanoscale Res. Lett. 6 (2011) 615.

[53] L. Sangaletti, L.E. Depero, B. Allieri, F. Pioselli, E. Comini, G. Sberveglieri, M. Zocchi, Oxidation of Sn Thin Films to SnO_2. Micro-Raman Mapping and X-ray Diffraction Studies, J. Mater. Res. 13 (2011) 2457–2460.

[54] Y. Wei, J. Liu, F. Cheng, J. Chen, Mn-doped atomic SnO_2 layers for highly efficient CO_2 electrochemical reduction, J. Mater. Chem. A 7 (2019) 19651–19656.

[55] A.A. Peterson, J.K. Nørskov, Activity descriptors for CO_2 electroreduction to methane on transition-metal catalysts, J. Phys. Chem. Lett. 3 (2012) 251–258.

[56] X. Zheng, Y. Ji, J. Tang, J. Wang, B. Liu, H.-G. Steinrück, K. Lim, Y. Li, M.F. Toney, K. Chan, Y. Cui, Theory-guided Sn/Cu alloying for efficient CO_2 electroreduction at low overpotentials, Nat. Catal. 2 (2018) 55–61.

[57] J.T. Feaster, C. Shi, E.R. Cave, T. Hatsukade, D.N. Abram, K.P. Kuhl, C. Hahn, J. K. Nørskov, T.F. Jaramillo, Understanding selectivity for the electrochemical reduction of carbon dioxide to formic acid and carbon monoxide on metal electrodes, ACS Catal. 7 (2017) 4822–4827.

[58] J.S. Yoo, R. Christensen, T. Vegge, J.K. Nørskov, F. Studt, Theoretical insight into the trends that guide the electrochemical reduction of Carbon Dioxide to formic acid, ChemSusChem 9 (2016) 358–363.